MRS Communications (2017), 7, 715–720
© Materials Research Society, 2017
doi:10.1557/mrc.2017.77

MRS Communications

Research Letter

TaWSi amorphous metal thin films: composition tuning to improve thermal stability

John M. McGlone, Department of Electrical Engineering and Computer Science, Oregon State University, Corvallis, Oregon 97331-5501, USA
Kristopher R. Olsen†, Department of Chemistry, Oregon State University, 153 Gilbert Hall, Corvallis, Oregon 97331-4003, USA
William F. Stickle, Hewlett-Packard Company, Corvallis, Oregon 97333, USA
James E. Abbott, 3D NanoColor, 1110 NE Circle Blvd, Corvallis, Oregon 97330, USA
Roberto A. Pugliese and **Greg S. Long,** Hewlett-Packard Company, Corvallis, Oregon 97333, USA
Douglas A. Keszler, Department of Chemistry, Oregon State University, 153 Gilbert Hall, Corvallis, Oregon 97331-4003, USA
John F. Wager, Department of Electrical Engineering and Computer Science, Oregon State University, Corvallis, Oregon 97331-5501, USA
Address all correspondence to John M. McGlone at **johnmmcglone@gmail.com** and **mcglonej@oregonstate.edu**

(Received 12 June 2017; accepted 17 August 2017)

Abstract

We deposited TaWSi amorphous metal thin films to determine how composition affects film crystallization and oxidation at high temperatures. Films were deposited by magnetron sputtering from targets of nominal compositions Ta : W : Si = 40 : 40 : 20, 30 : 50 : 20, and 30 : 30 : 40, and studied by electron probe microanalysis, electron microscopy, electrical methods, x-ray diffraction, x-ray photoelectron spectroscopy, and atomic-force microscopy. All films remained amorphous to 800 °C or higher temperatures. Films prepared from the target composition 30 : 30 : 40 yielded the film composition $Ta_{41.7}W_{38.4}Si_{19.9}$, which retained its film integrity and amorphous structure to 1100 °C, even after annealing in air.

Introduction

Numerous applications require thermally robust metal thin films that possess both high strength and corrosion resistance. Examples of high-temperature applications include thermal inkjet printing,[1] pressure sensors in combustion engines,[2] and turbine blade protective coatings.[3] Semiconductor manufacturing also requires thermal stability of metals to 400 °C for back-end-of-line processing[4] and above 1000 °C for gate metal annealing.[5]

An amorphous metal thin film (AMTF) is an attractive option for such applications. It lacks the grain boundaries and dislocations of crystalline materials, which degrade mechanical strength and provide pathways for chemical attack. Additionally, an amorphous thin film possesses an ultra-smooth surface when deposited onto a substrate with a smooth surface, a feature that often enhances device performance. These attributes have stimulated interest in their use for many emerging applications.[6,7]

Amorphous metals are metastable and prone to crystallize at high temperatures. Once crystallized, their performance advantages are lost. We examine here how to produce new refractory amorphous thin films with high crystallization and oxidation temperatures.

Amorphous metals comprising refractory elements, such as Ta, W, or both, are expected to crystallize at high temperatures, since the crystallization temperature of an amorphous metal depends on the melting point of its constituent elements.[8] Compositions with metalloids, such as Si, further enhance high-temperature stability. The metalloid contributes to large negative heats of mixing, increases atomic-size diversity, and forms strong bonds with the refractory metals, all factors that increase the high-temperature stability of the amorphous structure.[9,10] Refractory amorphous alloys that employ these features have crystallization temperatures ranging from 800 to over 1100 °C.[11–14]

We describe herein the properties of three new refractory AMTFs derived from the target compositions $Ta_{40}W_{40}Si_{20}$, $Ta_{30}W_{50}Si_{20}$, and $Ta_{30}W_{30}Si_{40}$. These compositions were chosen to systematically examine the effects of both refractory metal and metalloid content across a narrow range to suppress crystallization. The structures, electrical properties, and thermal stabilities of these films are compared with those of sputtered Ta thin films.

Experimental

Dense 2-in. metal targets of nominal composition $Ta_{40}W_{40}Si_{20}$, $Ta_{30}W_{50}Si_{20}$, and $Ta_{30}W_{30}Si_{40}$ were purchased from Materion. Thin films were deposited by magnetron sputtering onto 25-mm^2 Si/SiO_2 substrates at a base pressure $<10^{-6}$ Torr.

† These authors share first authorship.

https://doi.org/10.1557/mrc.2017.77 Published online by Cambridge University Press

Thin films were sputtered at 100 W RF power and sputtering pressures from 5 to 20 mTorr. The substrate to target throw distance was set to 4 in. and no substrate bias, cooling, or heating were applied. $Ta_{40}W_{40}Si_{20}$, $Ta_{30}W_{50}Si_{20}$, and $Ta_{30}W_{30}Si_{40}$ thin films were sputtered at rates near 7, 10, and 8 nm/min, respectively, to a thickness of approximately 200 nm, which was confirmed with an Alpha-Step 500 Surface Profilometer. Unless stated otherwise, measurements were made on the 200-nm-thick films. Resistivity was assessed from film thickness and resistance measured with a Jandel RM-2 collinear four-point probe.

Transmission electron microscopy (TEM) and convergent beam electron diffraction (CBED) experiments were performed with a FEI Titan 80-200 TEM/STEM. TEM samples were first coated with amorphous carbon (*a*-C) and chromium before being sectioned for analysis. CBED analysis was performed with a converged beam size of 50–200 nm^2. Surface roughness and morphology were determined by atomic-force microscopy (AFM) with an Asylum atomic-force microscope operating in contact mode. Scanning electron microscope (SEM) images were acquired with an FEI Helios 650 dual beam SEM operating in immersion mode with a circular backscatter detector.

Crystallization temperatures were measured after heating samples in evacuated (20–50 mTorr), sealed fused-silica tubes, at selected temperatures between 800 and 1100 °C. The tubes were heated at 5 °C/min with 20-min dwell at the final temperature. Grazing-incidence x-ray diffraction (GI-XRD) data were acquired with a Rigaku Ultima-IV x-ray diffractometer equipped with a thin-film stage.

Film compositions were determined by electron probe microanalysis (EPMA) with a Cameca SX100 electron probe micro-analyzer. Films were deposited on Cu substrates for analysis.

X-ray photoelectron spectroscopy (XPS) measurements were made with a PHI Quantera Scanning ESCA spectrometer equipped with a monochromatic Al x-ray source having a photon energy of 1486.6 eV. The data were charge-corrected to carbon 1s at 284.8 eV. The binding energy (BE) scale was calibrated with the Cu $2p_{3/2}$ feature at 932.7 ± 0.05 eV and Au 4*f* at 84.0 ± 0.05 eV. Compositions were determined by using standard elemental relative sensitivity factors corrected for the transmission function of the analyzer. Sputter depth profiles were acquired by alternately sputtering and acquiring spectral data. Samples were sputtered with a 2-kV Ar^+ ion beam at a sputter rate of ~5 nm/min relative to SiO_2. The sputter depth-profile data were reduced by using a linear least-squares method to separate overlap of the Ta 4*f* and the O 2*s* signals and to assign the chemical state of silicon to silicide or oxide.[15]

Results and discussion

Structure, electrical properties, and composition

Figure 1(a) shows GI-XRD patterns for $Ta_{40}W_{40}Si_{20}$, $Ta_{30}W_{50}Si_{20}$, and $Ta_{30}W_{30}Si_{40}$ thin films. The broad features from approximately 35° to 45° and 60° to 75° are indicative

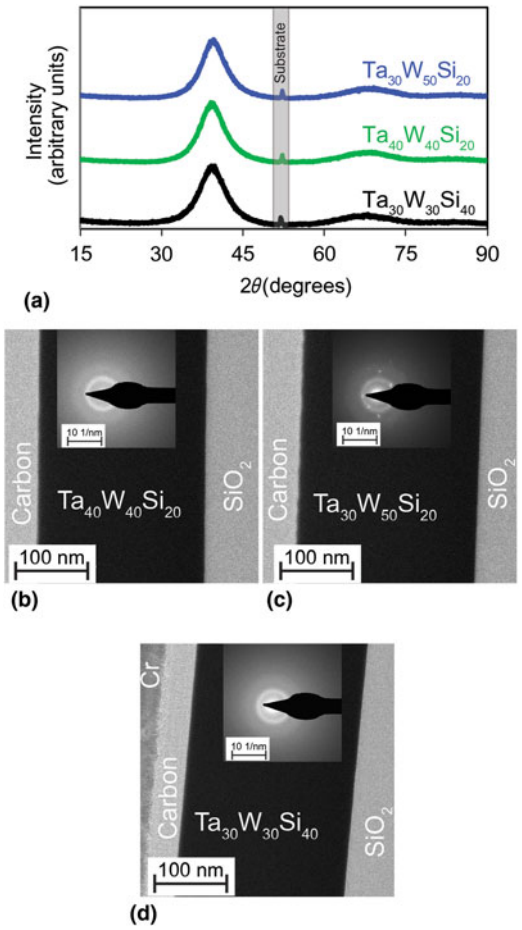


Figure 1. (a) As-deposited GI-XRD patterns for thin films of $Ta_{40}W_{40}Si_{20}$, $Ta_{30}W_{50}Si_{20}$, and $Ta_{30}W_{30}Si_{40}$ with the silicon substrate peak identified. TEM cross-section and convergent beam electron diffraction (CBED) pattern of a (b) $Ta_{40}W_{40}Si_{20}$, (c) $Ta_{30}W_{50}Si_{20}$, and (d) $Ta_{30}W_{30}Si_{40}$ thin film. Diffraction analysis of $Ta_{40}W_{40}Si_{20}$ and $Ta_{30}W_{30}Si_{40}$ confirms the amorphous structure and shows no evidence of crystallinity in the thin film. Diffraction analysis of $Ta_{30}W_{50}Si_{20}$ confirms the structure to be amorphous with a small fraction of nanocrystalline domains embedded in the amorphous structure.

of an amorphous thin film. The absence of Bragg reflections, i.e., sharp, distinctive peaks, indicates a lack of long-range crystalline order. Figures 1(b), 1(c), and 1(d) show CBED patterns for the three compositions. The patterns for $Ta_{40}W_{40}Si_{20}$ and $Ta_{30}W_{30}Si_{40}$ exhibit diffuse halos, which confirm the amorphous character of the films. Similarly, the pattern for $Ta_{30}W_{50}Si_{20}$ shows diffuse halos, but also sharp spots. These spots represent nanocrystalline domains of WSi_2[16] embedded in an environment of amorphous metal. From the high-resolution TEM image and the lack of diffraction peaks in the GI-XRD pattern, we estimate the diameter of the nanocrystallites to be <4 nm. Considering the small grain size and apparent low concentration of the crystallites, we consider the samples to be substantially amorphous.

Table I summarizes surface roughness, resistivity, and composition for each film as-deposited. The root-mean-square

https://doi.org/10.1557/mrc.2017.77 Published online by Cambridge University Press

Table I. Properties of as-deposited TaWSi thin films.

Target	Film roughness (RMS, nm)	Film resistivity (μΩ cm)	Film composition[a]
$Ta_{40}W_{40}Si_{20}$	0.3	199 ± 10	$Ta_{45.3}W_{43.7}Si_{11.0}$
$Ta_{30}W_{50}Si_{20}$	0.5	201 ± 6	$Ta_{35.4}W_{53.3}Si_{11.3}$
$Ta_{30}W_{30}Si_{40}$	0.25	218 ± 5	$Ta_{41.7}W_{38.4}Si_{19.9}$

[a]Film composition estimated via EPMA, neglecting oxygen (≤5%).

(rms) surface roughness, determined by AFM, is <0.5 nm for each film. The ultra-smooth nature of the surfaces further characterizes the films as amorphous. The room temperature resistivities are all ~200 μΩ cm, which is in the range expected for an amorphous metal. Note that the resistivity of an amorphous metal is expected to be higher than that of its constituent crystalline elements.[9] Typical sputtered β-Ta, α-Ta, and W thin films possess resistivities of 165, 25, and 14 μΩ cm, respectively.[17,18]

The Si concentration in all of the TaWSi thin films is lower than that of the target. We find that Si is preferentially deposited off-axis onto the sputter chamber walls. Other researchers have previously reported that magnetron sputtering with a multicomponent target may result in a thin-film composition different from that of the target.[19,20] For example, sputtered WTi[21] and WSi[22] thin films exhibit a reduced concentration of the lighter element, Ti and Si, respectively, compared with that of the target. These results are consistent with the compositional trends of the films.

Figure 2 shows an XPS composition and chemical-state depth profile of a 200-nm-thick $Ta_{40}W_{40}Si_{20}$ thin film. For XPS composition and chemical-state depth profiles of $Ta_{30}W_{50}Si_{20}$ and $Ta_{30}W_{30}Si_{40}$ thin films, see Supplementary Figs. S1(a) and S1(b), respectively. The depth profiles demonstrate that the elemental distribution of Ta, W, and Si is uniform throughout the bulk of the thin film. Note that the atomic ratios in Fig. 2 cannot be compared directly with the composition established by EPMA, as the compositional depth profile has not been corrected for preferential sputtering. The data also show that Si is present as silicide, which is also consistent with the low, observed O content.

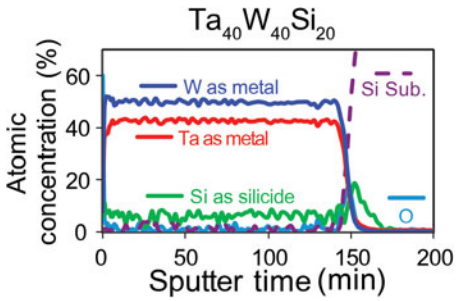


Figure 2. XPS composition sputter depth profile of a $Ta_{40}W_{40}Si_{20}$ thin film showing uniform composition throughout the bulk of the film. Atomic concentrations are not corrected for preferential sputtering.

Thermal studies

Figure 3 shows GI-XRD patterns of $Ta_{40}W_{40}Si_{20}$, $Ta_{30}W_{50}Si_{20}$, and $Ta_{30}W_{30}Si_{40}$ thin films as-deposited and heated in 100 °C increments to 1100 °C in evacuated, sealed silica tubes. The broad features in the patterns of $Ta_{40}W_{40}Si_{20}$ [Fig. 3(a)] indicate that the film remains amorphous to 900 °C. At 1000 °C, the broad features change to sharp Bragg reflections arising from crystalline material. The remaining diffuse background indicates an amorphous fraction remains at this temperature and annealing time. At 1100 °C, the amorphous contribution reduces as the Bragg intensities increase because of additional crystal growth. Phase analysis shows the crystalline material to be W_5Si_3 (see Supplementary Fig. S2).

Figure 3(b) shows $Ta_{30}W_{50}Si_{20}$ to be amorphous at 800 °C. At 900 °C, a new sharp peak appears near 42°, indicating the film begins to crystallize. As the temperature increases to 1000 °C, the intensity of this peak grows, while the broad diffuse background intensity decreases. The diffraction peaks at 900 and 1000 °C are consistent with elemental W or a TaW solid solution [see Supplementary Fig. S3(a)]. After the 1100 °C anneal, the thin film undergoes additional reaction and grain growth to form a mixture of crystalline W_5Si_3 and WSi_2 [see Supplementary Fig. S3(b)].

Figure 3(c) shows the GI-XRD patterns for $Ta_{30}W_{30}Si_{40}$ change little up to 1000 °C; they exhibit only broad peaks consistent with an amorphous structure. At 1100 °C, sharp Bragg peaks emerge that match those of W or a WTa solid solution (see Supplementary Fig. S4). If the temperature were further increased, we expect a silicide phase to form.

To summarize, the x-ray data show crystalline W (or TaW) separates from $Ta_{30}W_{50}Si_{20}$ above 800 °C. This W segregation is suppressed with the smaller W content in $Ta_{40}W_{40}Si_{20}$. This material clearly crystallizes as a mixture of silicides at 1000 °C. The increased Si content of $Ta_{30}W_{30}Si_{40}$ then suppresses both silicide and W (TaW) formation, increasing the crystallization onset to temperatures above 1000 °C. Consequently, the crystallization temperature of the $Ta_{30}W_{30}Si_{40}$ system is similar to that of quaternary amorphous metal systems based on Ta, W, Si, and C,[11,12] which are among the higher reported crystallization temperatures for amorphous metals. TaWSi provides

https://doi.org/10.1557/mrc.2017.77 Published online by Cambridge University Press

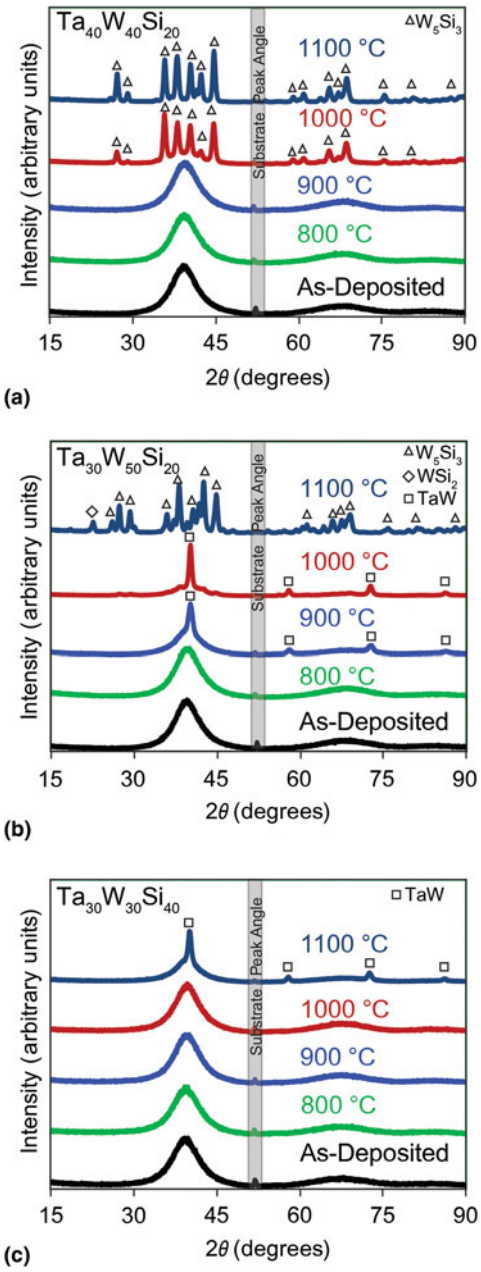


Figure 3. XRD patterns from (a) $Ta_{40}W_{40}Si_{20}$, (b) $Ta_{30}W_{50}Si_{20}$, and (c) $Ta_{30}W_{30}Si_{40}$ thin films as-deposited and after post-deposition annealing. The silicon substrate peak at ~52.5° is indicated.

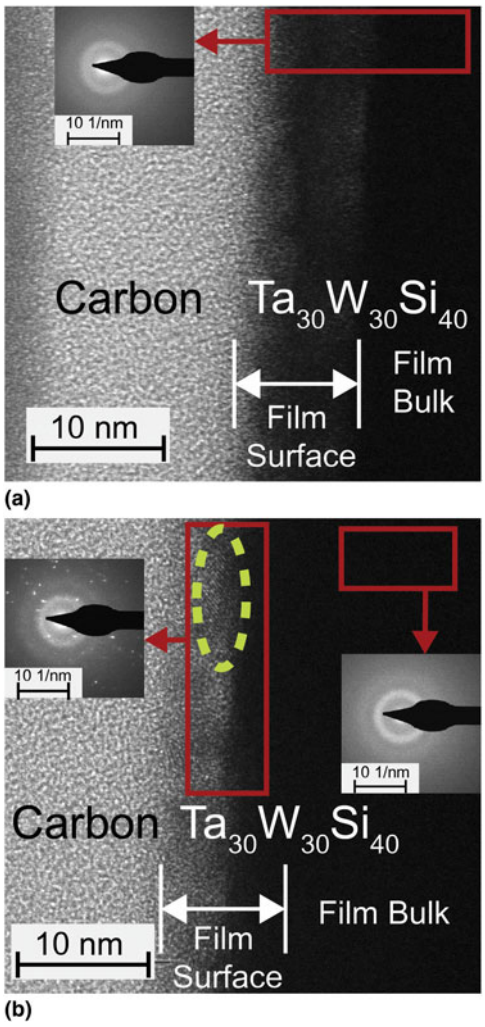


Figure 4. (a) TEM image of the near-surface region of a $Ta_{30}W_{30}Si_{40}$ thin film after a 1000 °C anneal with CBED pattern (inset). (b) TEM image of near-surface region of a $Ta_{30}W_{30}Si_{40}$ thin film after a 1100 °C anneal with corresponding CBED patterns from the surface (left) and bulk (right) regions of the thin film. The yellow dashed circle highlights the crystalline region. An amorphous carbon layer was deposited on the thin films for protection during the FIB process.

advantages under some conditions, as C commonly migrates from metals at high temperatures.

Figure 4(a) shows a TEM image and a CBED pattern for the near-surface region of the most thermally stable film composition, i.e., $Ta_{30}W_{30}Si_{40}$, after a 1000 °C anneal. The TEM image reveals the film to be continuous and smooth. No interactions are observed between the substrate and the thin film as seen in Supplementary Fig. S5 in the supplemental section. The diffuse rings in the CBED pattern confirm that the film remains amorphous after the anneal both near the surface and throughout the entire bulk of the thin film. Image contrast between the area labeled "film surface" and the bulk of the film indicates that the near-surface region is less dense than the film bulk. This low-density region indicates that the film forms an oxide cap by reaction with the residual oxygen in the sealed tube.

Figure 4(b) shows a TEM image and CBED patterns for the near-surface and bulk regions of the same $Ta_{30}W_{30}Si_{40}$ composition after annealing at 1100 °C. The TEM image indicates that the film remains continuous and smooth at 1100 °C. The image displays distinct lattice features at the carbon–metal interface consistent with crystal formation. The CBED pattern of this interface region exhibits bright diffraction spots, also consistent

https://doi.org/10.1557/mrc.2017.77 Published online by Cambridge University Press

with crystal formation. The bulk of the film remains amorphous, as indicated by the diffuse halos in the CBED image [right in Fig. 4(b)]. The TEM images and CBED patterns confirm that the $Ta_{30}W_{30}Si_{40}$ film remains amorphous to 1000 °C. Furthermore, they show a crystalline material preferentially nucleates and grows at the film surface.

Figure 5 shows plots of surface roughness versus annealing temperature for the three TaWSi thin-film compositions. Each film is 200-nm thick and AFM surface topography images are available in the supplemental data. Below 900 °C, each film exhibits a surface roughness of a few tenths of an nm, i.e., near the noise floor of the AFM instrument. This smoothness reflects the amorphous nature of the films. Above 900 °C, the surfaces of $Ta_{40}W_{40}Si_{20}$ and $Ta_{30}W_{50}Si_{30}$ roughen considerably, with the roughness rising to 4.65 nm at 1000 °C for $Ta_{40}W_{40}Si_{20}$ and 3.2 nm at 1100 °C for $Ta_{30}W_{50}Si_{30}$. The temperature onsets for increased AFM roughness agree with phase-segregation and crystallization temperatures deduced from the x-ray data (see Fig. 3).

Considered design guidelines suggest stability to crystallization increases with rising refractory metal content.[8] For the TaWSi system, W has the highest melting point, 3422 °C, compared with Ta, 3020 °C, and Si, 1414 °C. We find, however, that the W-rich $Ta_{30}W_{50}Si_{20}$ thin film crystallizes approximately 100 °C lower than $Ta_{40}W_{40}Si_{20}$ with a similar Si content. Ouyang et al.[12] described a similar result, wherein a W-rich amorphous metal crystallizes at a lower temperature than that of a Ta-rich amorphous metal. These unexpected results may arise from the larger enthalpy of mixing for Ta and Si, −56 kJ/mol, compared with mixing of W and Si, −31 kJ/mol.[10]

An additional design rule suggests a metalloid composition of at least 20% considerably enhances amorphous-metal thermal stability.[9,11,12] Our study confirms this guideline, as increasing the silicon content in the sputter target from 20%, $Ta_0W_{40}Si_{20}$ (or $Ta_{30}W_{50}Si_{20}$), to 40%, $Ta_{30}W_{30}Si_{40}$, produces a composition with at least 20% Si. The high Si-content $Ta_{30}W_{30}Si_{40}$ thin film exhibits the highest crystallization temperature. The increase in thermal stability is due to silicon's negative heat of mixing, atomic-size diversity, and strong bonds with the refractory metals as discussed in the introduction.

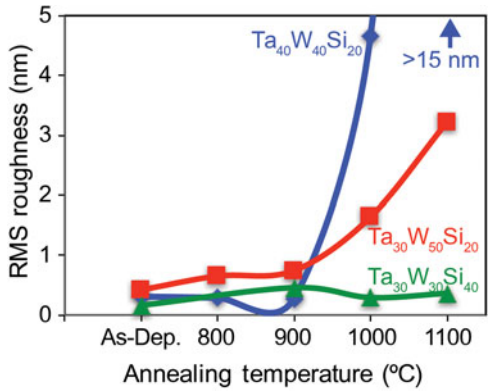


Figure 5. AFM roughness of $Ta_{40}W_{40}Si_{20}$, $Ta_{30}W_{50}Si_{20}$, and $Ta_{30}W_{30}Si_{40}$ thin films after annealing between 800 and 1100 °C.

Oxidation behavior

Thermally robust amorphous films are envisioned to replace sputtered Ta thin films in many applications. As-deposited, 200-nm-thick Ta films generally exhibit surface roughness >1 nm, which derives from the crystalline nature of the hexagonal, β-phase. Electrical resistivities near 165 μΩ cm reflect this crystalline nature.[17] Under vacuum or inert atmosphere, the β-phase transforms to the α-phase between 700 and 800 °C. Through this transition, the electrical resistivity drops to 25 μΩ cm,[17] and the rms surface roughness rapidly exceeds 2 nm as grain-growth occurs.

Figure 6(a) shows an SEM image of a 200-nm-thick Ta film after annealing in air at 700 °C for 10 min. Clearly, wide and deep cracks have compromised film integrity. Continued heating leads first to delamination, then conversion to Ta_2O_5 powder[23] and complete loss of film structure. Figure 6(b) shows an SEM image of a $Ta_{40}W_{40}Si_{20}$ thin-film surface under the same heating conditions. The film retains its smooth, featureless appearance after heating in air; oxidation negligibly affects film appearance and integrity. The rms surface

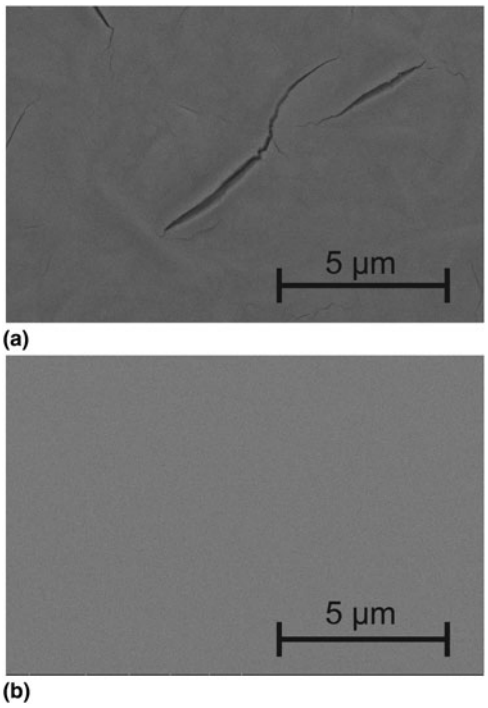


Figure 6. (a) SEM image of the surface of a 200-nm Ta thin film after a 700 °C anneal in air for 10 min. (b) SEM image of the surface of a 200-nm $Ta_{40}W_{40}Si_{20}$ thin film after a 700 °C anneal in air for 10 min.

https://doi.org/10.1557/mrc.2017.77 Published online by Cambridge University Press

roughness (0.3 nm) indicates that the film remains amorphous through the anneal. These results demonstrate the intrinsic advantages of the TaWSi formulation and its amorphous nature to produce a thermally robust, oxidation-resistant thin film that exceeds the performance characteristics of a crystalline Ta film.

Conclusions

Three new AMTFs from target compositions $Ta_{30}W_{50}Si_{20}$, $Ta_{40}W_{40}Si_{20}$, and $Ta_{30}W_{30}Si_{40}$ were deposited via magnetron sputtering. XRD, electron diffraction, AFM, and TEM analyses confirmed the films to be amorphous as deposited. Electrical measurements revealed resistivities, ~200 μΩ cm, consistent with the amorphous character. Crystallization temperature increased in the order $Ta_{30}W_{50}Si_{20} < Ta_{40}W_{40}Si_{20} < Ta_{30}W_{30}Si_{40}$. Each film exhibited stability to oxidation at temperatures above 700 °C, well above the oxidation temperature of Ta.

This study demonstrates the importance of refractory metal and metalloid contents for production of amorphous thin films that are thermally stable and resistant to oxidation at temperatures above 900 °C. Because commercial electronics already and widely employs Ta, W, and Si, tools and processes exist to integrate new and robust TaWSi films in the fabrication and manufacturing environments.[5]

Supplementary material

The supplementary material for this article can be found at https://doi.org/10.1557/mrc.2017.77

Acknowledgments

We thank the Hewlett Packard Company for financial support, Professor Brady Gibbons at Oregon State University (OSU) for the use of the AFM tool, Dr. Peter Eschbach and Teresa Sawyer in the OSU electron microscopy facility for assistance with TEM and SEM tools, and Julie Chouinard and John Donovan at the University of Oregon CAMCOR facility for assistance with EPMA measurements. This material is based upon the work supported by the National Science Foundation through the Major Research Instrumentation (MRI) Program under Grant No. 1040588. We also gratefully acknowledge financial support for the acquisition of the TEM instrument from the M. J. Murdock Charitable Trust and the Oregon Nanoscience and Microtechnologies Institute (ONAMI).

References

1. R.R. Allen, J.D. Meyer, and W.R. Knight: Thermodynamics and hydrodynamics of thermal ink jets. *Hewlett-Packard J.* **36**, 21 (1985).
2. M.A. Fonseca, J.M. English, M. von Arx, and M.G. Allen: Wireless micromachined ceramic pressure sensor for high-temperature applications. *J. Microelectromech. Syst.* **11**, 337 (2002). DOI: 10.1109/JMEMS.2002.800939.
3. G. Goward: Progress in coatings for gas turbine airfoils. *Surf. Coat. Technol.* **108–109**, 73 (1998). DOI: 10.1016/S0257-8972(98)00667-7.
4. A. Farcy, J.F. Carpentier, M. Thomas, J. Torres, and P. Ancey: Integration of high-performance RF passive modules (MIM capacitors and inductors) in advanced BEOL. *Microelectron. Eng.* **85**, 1940 (2008). DOI: 10.1016/j.mee.2008.03.017.
5. S. Wolf and R.N. Tauber: *Silicon Processing for the VLSI Era*, 2nd ed. (Lattice Press, Sunset Beach, CA, USA, 2000), vol. **1**.
6. J.P. Chu, J.S.C. Jang, J.C. Juang, H.S. Chou, Y. Yang, J.C. Yi, Y.C. Wang, J.W. Lee, F.X. Liu, P.K. Liaw, Y.C. Chen, C.M. Lee, C.L. Li, and C. Rullyani: Thin film metallic glasses: unique properties and potential applications. *Thin Solid Films* **520**, 5097 (2007). DOI: 10.1016/j.tsf.2012.03.092.
7. G. Kumar, A. Desai, and J. Schroers: Bulk metallic glass: the smaller the better. *Adv. Mater.* **23**, 461 (2011). DOI: 10.1002/adma.201002148.
8. X.Q. Zhang, E. Ma, and J. Xu, Mechanically alloyed multi-component Mo-based amorphous metals. *J. Non-Cryst. Solids* **352**, 3985 (2006). DOI: 10.1016/j.jnoncrysol.2006.07.041.
9. C. Suryanarayana and A. Inoue: *Bulk Metallic Glasses* (CRC Press Taylor and Francis Group, Boca Raton, FL, USA, 2011).
10. A. Takeuchi and A. Inoue: Calculations of mixing enthalpy and mismatch entropy for ternary amorphous alloys. *Mater. Trans., JIM* **41**, 1372 (2000). DOI: 10.2320/matertrans1989.41.1372.
11. M.E. Grubbs, X. Zhang, M. Deal, Y. Nishi, and B.M. Clemens, Development and characterization of high temperature stable Ta–W–Si–C amorphous metal gates. *Appl. Phys. Lett.* **97**, 223505 (2010). DOI: 10.1063/1.3508952.
12. J. Ouyang, R. Wongpiya, M.E. Grubbs, M.D. Deal, B.M. Clemens, and Y. Nishi: Effect of composition on structural and electrical properties of amorphous Ta–W–Si–C metal thin films. *ECS Solid State Lett.* **2**, 86 (2013). DOI: 10.1149/2.003310ssl.
13. T. Yoshitake, Y. Kubo, and H. Igarashi, Preparation of refractory transition metal-metalloid amorphous alloys and their thermal stability. *Mater. Sci. Eng.* **97**, 269 (1988). DOI: 10.1016/0025-5416(88)90055-9.
14. J.M. McGlone, K.R. Olsen, W.F. Stickle, J.E. Abbott, R.A. Pugliese, G. S. Long, D.A. Keszler, and J.F. Wager: Ta-based amorphous metal thin films. *J. Alloys Compd.* **650**, 102 (2015). DOI: 10.1016/j.jallcom.2015.07.226.
15. W.F. Stickle: The use of chemometrics in AES and XPS data treatment in surface analysis. In *Auger and X-Ray Photoelectron Spectroscopy*, edited by D. Briggs and J. Grant (IM Publications, Chichister, West Sussex, UK, 2003), pp. 377–398.
16. K. Tanaka, K. Nawata, H. Inui, M. Yamaguchi, and M. Koiwa: Refinement of crystallographic parameters in refractory metal disilicides. *Mat. Res. Soc. Symp. Proc.* **646**, N4-3 (2000). DOI: 10.1557/PROC-646-N4.3.1.
17. A. Schauer and M. Roschy: R.F. sputtered β-tantalum and B.C.C. tantalum films. *Thin Solid Films* **12**, 313 (1972). DOI: 10.1016/0040-6090(72)90095-8.
18. K. Bouziane, M. Mamor, and F. Meyer: DC magnetron sputtered tungsten: W film properties and electrical properties of W/Si Schottky diodes. *Appl. Phys. A* **81**, 209 (2005). DOI: 10.1007/s00339-004-2558-5.
19. B. Chapman: *Glow Discharge Processes* (John Wiley and Sons Inc, New York, 1980).
20. G. Betz and G.K. Wehner: Sputtering of multicomponent materials in sputtering. In *Particle Bombardment II: Sputtering of Alloys and Compounds, Electron and Neuron Sputtering, Surface Topography*, edited by R. Behrisch (Springer-Verlag, Berlin, 1983), pp. 42–48.
21. L.R. Shaginyan, M. Misina, S. Kadlec, and L. Jasterbi: Mechanisms of the film composition formation during magnetron sputtering of W Ti. *J. Vac. Sci. Technol. A* **19**, 2554 (2001). DOI: 10.1116/1.1392401.
22. Y. Murakami and T. Shingyoji: Compositional difference between films and targets in sputtering of refractory metal silicides. *J. Vac. Sci. Technol. A* **8**, 851 (1990). DOI: 10.1116/1.576929.
23. R. Chandrasekharan, I. Park, R.I. Masel, and M.A. Shannon: Thermal oxidation of tantalum films at various oxidation states from 300 to 700 °C. *J. Appl. Phys.* **98**, 114908 (2005). DOI: 10.1063/1.2139834.

https://doi.org/10.1557/mrc.2017.77 Published online by Cambridge University Press